

ERANet: Edge Replacement Augmentation for Semi-Supervised Meniscus Segmentation with Prototype Consistency Alignment and Conditional Self-Training

Siyue Li¹, Yongcheng Yao^{1,2}, Junru Zhong¹, Shutian Zhao¹, Fan Xiao³, Tim-Yun Michael Ong⁴, Ki-Wai Kevin Ho⁵, James F. Griffith¹, Yudong Zhang⁶, Shuihua Wang⁷, Jin Hong^{8,*}, Weitian Chen^{1,*}

¹ CU Lab for AI in Radiology (CLAIR), Department of Imaging and Interventional Radiology, The Chinese University of Hong Kong, Hong Kong, China.

² School of Informatics, University of Edinburgh, Edinburgh, Scotland, United Kingdom.

³ Department of Radiology, Shanghai Sixth People's Hospital Affiliated to Shanghai Jiao Tong University School of Medicine, Shanghai, China.

⁴ Department of Orthopaedics & Traumatology, The Chinese University of Hong Kong, Hong Kong, China.

⁵ Department of Orthopaedics & Traumatology, The Chinese University of Hong Kong Medical Centre, Hong Kong, China.

⁶ School of Computer Science and Engineering, Southeast University, Nanjing, China.

⁷ Department of Biological Sciences, School of Science, Xi'an Jiaotong Liverpool University, Suzhou, China.

⁸ School of Information Engineering, Nanchang University, Nanchang, China.

Email: siyueli@link.cuhk.edu.hk; yc.yao@ed.ac.uk; jrzong@link.cuhk.edu.hk; zhaoshutian@sjtu.edu.cn; freidaxiao@gmail.com; michael.ong@cuhk.edu.hk; kevinkiwaiho@gmail.com; griffith@cuhk.edu.hk; yudongzhang@ieee.org; Shuihua.Wang@xjtlu.edu.cn; hongjin@ncu.edu.cn; wchen@cuhk.edu.hk

* Correspondence should be addressed to Jin Hong & Weitian Chen

Abstract : The meniscus, a critical fibrocartilaginous structure within the knee joint, plays an essential role in maintaining knee functionality and mitigating degenerative changes associated with osteoarthritis (OA). Accurate and efficient segmentation of the meniscus in Magnetic Resonance Imaging (MRI) is crucial for early diagnosis and monitoring OA progression. However, manual segmentation is labor-intensive, and automatic segmentation remains challenging due to the inherent variability in meniscal morphology, partial volume effects, and low contrast between the meniscus and surrounding tissues. To address these challenges, we propose ERANet, an innovative semi-supervised framework for meniscus segmentation that effectively leverages both labeled and unlabeled images through advanced augmentation and learning strategies. ERANet integrates three key components: edge replacement augmentation (ERA), prototype consistency alignment (PCA), and a conditional self-training (CST) strategy within a mean teacher architecture. ERA introduces anatomically relevant perturbations by simulating meniscal variations, ensuring that augmentations align with the structural context. PCA enhances segmentation performance by aligning intra-class features and promoting compact, discriminative feature representations, particularly in scenarios with limited labeled data. CST improves segmentation robustness by iteratively refining pseudo-labels and mitigating the impact of label noise during training. Together, these innovations establish ERANet as a robust and scalable solution for meniscus segmentation, effectively addressing key barriers to practical implementation. We validated ERANet comprehensively on 3D Double Echo Steady State (DESS) and 3D Fast/Turbo Spin Echo (FSE/TSE) MRI sequences. The results demonstrate the superior performance of ERANet compared to state-of-the-art methods. The proposed framework achieves reliable and accurate segmentation of meniscus structures, even when trained on minimal labeled data. Extensive ablation studies further highlight the synergistic contributions of ERA, PCA, and CST, solidifying ERANet as a transformative solution for semi-supervised meniscus segmentation in medical imaging.

Keywords: Meniscus segmentation, Magnetic Resonance Imaging, semi-supervised learning, data augmentation, prototype consistency learning.

1. Introduction

Osteoarthritis (OA) is a common and debilitating condition characterized by pain, stiffness, and disability, particularly in older adults [1]. Early detection and intervention are essential for managing OA and mitigating its long-term effects [2-4]. The meniscus, a crescent-shaped fibrocartilaginous structure within the knee joint, plays a critical role in shock absorption and load distribution between the femur and tibia [5]. Maintaining its structural integrity is vital for preserving knee function and preventing degenerative changes, as meniscal damage is strongly linked to the development of knee OA [6, 7]. Due to its key biomechanical functions, the meniscus is often one of the first knee structures to exhibit degeneration or injury during OA progression [8]. Accurate and reliable segmentation and quantification of the meniscus are crucial for tracking its morphological and compositional changes over time, facilitating early diagnosis and monitoring of disease progression.

Magnetic Resonance Imaging (MRI) has emerged as a pivotal diagnostic tool for the detailed multi-planar assessment of the body's internal structures, owing to its ability to represent diverse soft tissue contrasts. Specifically for the meniscus, MRI offers advantages over CT and X-ray, which are only optimized for imaging dense structures such as bone [9]. MRI enables the precise depiction of subtle meniscal changes—such as tears, degeneration, extrusion, and thinning—without the use of ionizing radiation [10]. However, meniscus segmentation on MRI remains challenging due to factors like low contrast between the meniscus and surrounding tissues, partial volume effects, variability in meniscal morphology, and its small size. Manual segmentation, while feasible, is time-intensive, requires specialized expertise, and is susceptible to inter- and intra-observer variability. With advancements in deep learning (DL) methods, fully supervised DL networks [11-15] have been developed to tackle the meniscus segmentation problem. Despite achieving satisfactory results, these models share a common limitation: they require a substantial amount of annotated data for effective training. To mitigate these challenges, semi-supervised networks, which combine a small amount of labeled data with a larger pool of unlabeled data during training, have been employed [16].

The key challenge in semi-supervised segmentation lies in effectively leveraging unlabeled images to extract useful information that complements a limited labeled dataset. Existing approaches in semi-supervised segmentation broadly fall into two categories: entropy minimization and regularization-based methods. Entropy minimization aims to reduce uncertainty in model predictions on unlabeled data, promoting confident and discriminative outputs [17]. Self-training (ST), a widely adopted approach for entropy minimization [18-21] leverages pseudo-labeling to iteratively refine model predictions. This process progressively reduces uncertainty by focusing on high-confidence predictions. However, pseudo-labeling is susceptible to error propagation, as incorrect pseudo labels may reinforce inaccuracies during training, undermining model reliability. Recent advancements have focused on regularization-based methods, including generative model-based adversarial learning [22-24], consistency learning [25-27], and co-training [28-30]. These methods aim to improve segmentation accuracy by effectively utilizing both labeled and unlabeled data. Consistency-based approaches are particularly popular due to their simplicity and strong performance in many studies. However, most consistency learning methods rely on data perturbation, applying random changes to unlabeled data without direct guidance from true labels. This can be problematic, as generic perturbations may not be suitable for all tasks. Minor perturbations may weaken the consistency loss by failing to impact the predicted results meaningfully.

Prototypical segmentation methods have recently gained attention for leveraging unlabeled images by focusing on reducing intra-class variability and enhancing inter-class separability. These methods employ prototypical feature representations, aligning pixel-level features with learned class prototypes to generate pseudo labels. Consistency regularization is applied, based on the assumption that features from the same class should cluster around their prototype while remaining distant from prototypes of other classes. Wu et al. [31] proposed an approach utilizing image-level prototypes derived from labeled data, which are transferred to unlabeled data through a global model for pseudo label generation via consistency learning. Their dynamic consistency-aware aggregation strategy adjusts the weights of local model contributions to the global model dynamically, further refining segmentation performance. However, challenges arise in medical imaging due to the grayscale nature and limited textural information of many images. These characteristics often lead to overlapping prototypes across different categories, making prototype contrastive learning more complex and demanding.

In this study, we present a novel semi-supervised approach for meniscus segmentation from MR images. Our method introduces an advanced edge replacement augmentation-based framework, **ERANet**, which integrates the mean teacher (MT) [32] architecture with edge replacement augmentation (ERA), prototype consistency alignment (PCA), and a conditional ST (CST) strategy. ERA generates data perturbation for consistency learning while tailoring it specifically for meniscus segmentation. This is achieved by simulating variations in meniscus shape and inflammation, replacing its marginal areas with background information from the same image. This form of augmentation ensures the perturbations remain contextually relevant to the meniscus structure. Additionally, PCA enhances intra-class similarity by computing correlations between learned prototypes and feature maps, thereby promoting intra-class compactness within unlabeled data. Furthermore, we incorporate a CST strategy that mitigates performance degradation caused by incorrect pseudo labels. Conditional retraining focuses on reliable unlabeled data, identified through confidence in the training process, ensuring more robust and accurate segmentation.

We validated the proposed method on two datasets acquired using 3D Double Echo Steady State (DESS) and 3D Fast/Turbo Spin Echo (FSE/TSE) sequences, respectively. Due to the short T2 relaxation time of the meniscus and different echo times used in these pulse sequences, the contrast between the meniscus and the surrounding tissues is highly different in DESS and FSE images, with the meniscus being visible in DESS but dark in FSE

images. Such contrast discrepancy demonstrates the generation potential of the proposed approach.

Our contributions are summarized as follows:

- i. We propose a novel semi-supervised meniscus segmentation framework, ERANet, which integrates a newly designed augmentation method ERA, PCA, and a CST strategy. This framework significantly improves the segmentation accuracy of meniscus tissues with limited labeled data and achieves superior performance compared to state-of-the-art semi-supervised methods on datasets acquired using two different MRI pulse sequences.
- ii. The ERA effectively simulates meniscus variations by mimicking the structural diversity of target tissues. By generating contextually appropriate data perturbations for meniscus MR images, ERA enhances segmentation performance, particularly for medial meniscus structures which are prone to injury and deformation.
- iii. The introduction of PCA aligns feature representations from unlabeled samples, emphasizing intra-class feature matching. This fosters compact and discriminative feature representations, enabling better generalization in semi-supervised scenarios. Consequently, this approach significantly boosts segmentation accuracy, especially when annotated data is scarce.
- iv. The CST strategy iteratively refines pseudo labels to improve segmentation performance. By progressively optimizing the model with both manually labeled and pseudo-labeled images, CST mitigates the impact of noisy pseudo labels. This refinement ensures robust learning from reliable unlabeled data, outperforming traditional self-training approaches consistently.
- v. Our extensive ablation studies demonstrate the synergistic effects of ERA, PCA, and CST in achieving robust performance across varying annotation levels. These techniques ensure reliable segmentation, achieving state-of-the-art results on datasets acquired using different MRI pulse sequences, even with sparse labeled data.

2. Related Work

2.1 meniscus segmentation

Since the introduction of the UNet [33] architecture in 2015, medical image segmentation, including meniscus segmentation, has seen significant advancements. Multiple studies (e.g., [11, 12, 34-37]) have applied DL approaches, often augmented with post-processing techniques such as conditional random fields and statistical shape models, to enhance segmentation precision. Notably, [12] demonstrated strong concordance between manual and automated segmentation-derived quantifications for T1 ρ and T2 relaxation times of meniscus. Similarly, [35] reported moderate correlations between automated and manual assessments of medial meniscal extrusion, reflecting the utility of DL networks in clinical evaluations. Adversarial learning has emerged as a powerful strategy for meniscus segmentation [14, 38]. Generative adversarial networks (GANs) are particularly well-suited for improving sensitivity to both global and local features, a critical requirement for accurately segmenting the meniscus's thin and irregular structure. For instance, [38] employed a conditional GAN framework, and [14] explored conditional GANs for both cartilage and meniscus segmentation, incorporating UNet-based pre-localization to generate object-aware maps that effectively address class imbalance issues. These adversarial learning methods excel by iteratively refining segmentation results: they prevent under-segmentation through repeated quality assessments and enhance focus on meniscus regions to mitigate over-segmentation, often using task-specific attention mechanisms.

The aforementioned methods for meniscus segmentation rely heavily on extensive labeled training datasets, presenting significant challenges due to the labor-intensive and costly nature of manual annotation. To mitigate these limitations, transfer learning and semi-supervised learning approaches have been explored. For instance, [39] developed an attention-based 2D UNet, leveraging a model pre-trained on a large non-medical image dataset and fine-tuning it on a smaller MRI dataset of meniscus. While this approach showed promise, it still required sizable labelled data. Semi-supervised learning strategies have sought to further reduce labeling requirements. For example, [40] proposed a modified UNet to perform semi-supervised segmentation on 3D DESS MRI datasets. In a related context, weakly supervised learning has also been investigated, as exemplified by [41], who utilized masked autoencoders pre-trained in a self-supervised manner. This method employed sparse annotations, such as points and lines, to guide the segmentation model, thereby reducing the overall annotation workload. Nevertheless, these methods either continue to depend on sizable annotated datasets or require additional forms of sparse labeling, which constrains their scalability in practice.

Moreover, most existing research focuses on a single MRI sequence, limiting its adaptability to different imaging

protocols. To address these challenges, we propose ERANet, an innovative semi-supervised framework designed for meniscus segmentation. By reducing annotation requirements to as little as 10%, ERANet ensures efficient data utilization and robust performance. Furthermore, validation across two widely used MRI sequences underscores its enhanced generalizability and potential clinical applicability.

2.2 semi-supervised segmentation

The field of semi-supervised semantic segmentation has made significant progress by leveraging advancements in general semi-supervised learning (SSL) techniques across various tasks. These developments have proven effective in mitigating the challenges associated with extensive annotation requirements. GAN-based adversarial learning approaches aim to align the output distributions of labeled and unlabeled data by enforcing consistency between their segmentation predictions. However, GANs are difficult to train due to their adversarial optimization process, often suffering from instabilities and mode collapse. Recent advancements in semi-supervised semantic segmentation have progressed from GAN-based methods to consistency regularization, emphasizing prediction stability under perturbations, such as strong-weak augmentations and network-level variations like model initialization or architecture changes.

[42] explored retinal vessel segmentation by integrating an MT mechanism as auxiliary consistency regularization with GANs. This approach introduced "leaking perturbation," allowing "leaking links" from the generator to the discriminator, which encouraged the generator to produce more moderate, albeit less realistic, outputs. [26] introduced a mutual consistency network for left atrium segmentation, leveraging two distinct decoders to estimate and minimize prediction discrepancies through a cyclic pseudo-labeling scheme. This framework enforces consistency between decoders, driving low-entropy predictions and fostering the gradual extraction of generalized features from unlabeled data. CPS [43] utilizes two parallel networks with distinct initializations to generate cross pseudo labels, a method proven effective in cardiac[44, 45], left atrium[44], and prostate[45] segmentation tasks. [46] proposed a bidirectional copy-paste augmentation strategy to mitigate the empirical distribution mismatch between labeled and unlabeled data. This approach transfers random crops between labeled and unlabeled images within an MT framework, fostering shared semantic learning and bridging distribution gaps. While effective in various domains, such consistency-based methods relying on random augmentations may not be optimal for meniscus segmentation due to the small size and shape variability of the meniscus.

Recently, prototype-based methods have been introduced in semi-supervised semantic segmentation to address the challenge of intra-class variation, which impedes label propagation between pixels [47]. [48] introduced cyclic prototypical networks with consistency learning to enhance robust, well-separated prototype representations for segmentation targets, integrating contextual information from labeled and unlabeled data through masked average pooling. [31] explored the use of image-level prototypes from labeled datasets transferred to unlabeled clients for prototypical contrastive learning, enhancing discriminative power and enabling dynamic model aggregation in federated semi-supervised segmentation. [49] investigated a self-aware and cross-sample prototypical learning method to enhance prediction diversity in consistency learning, integrating a novel dual loss that addresses both intra-class compactness and inter-class discrepancy, thereby improving semantic information utilization across multiple inputs. However, prior research has largely neglected the consideration of the stability and sensitivity of prototypical prediction results in response to perturbations within the consistency learning framework. Additionally, recent studies have revisited ST techniques for semi-supervised segmentation tasks [50-53], demonstrating their potential in leveraging pseudo labels to improve model performance. [50] and [53] underscore the critical role of strong data perturbations in enhancing the effectiveness of ST. However, these strategies have largely been limited to natural image segmentation. To bridge this gap, we propose ERANet, incorporating a novel ERA technique designed specifically for meniscus segmentation. The framework further integrates prototype consistency alignment and CST strategies to address challenges posed by the intricate structural features and variability of the meniscus in medical imaging.

3. Method

3.1 The semi-supervised segmentation framework

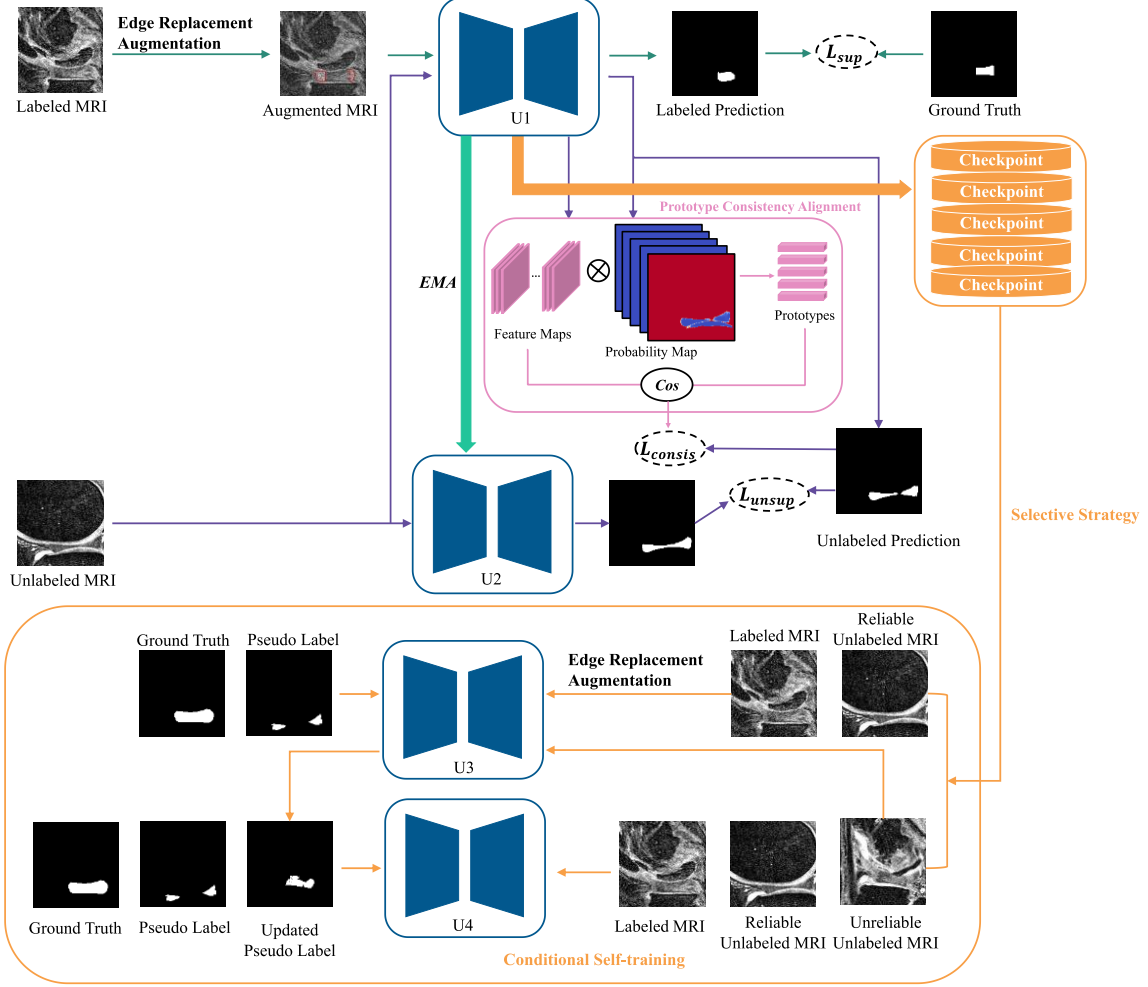


Figure 1. Architectural overview of ERANet, a semi-supervised meniscus segmentation framework leveraging both labeled and unlabeled images. ERANet comprises four segmentation networks ($U1$, $U2$, $U3$, and $U4$), optimized through mean-teacher training, prototype consistency alignment, conditional self-training, and edge replacement augmentation. $U1$ is trained using a combination of supervised loss on labeled images, unsupervised loss on unlabeled images, and consistency loss derived from prototypical predictions on the unlabeled samples. $U2$ represents the Exponential Moving Average (EMA) of the $U1$ model. $U3$ and $U4$ are trained using both labeled and pseudo-labeled images. A selective strategy filters reliable unlabeled images, enabling effective conditional self-training and improving segmentation accuracy.

In this section, we introduce ERANet, a novel framework designed for semi-supervised meniscus segmentation, with its architectural overview depicted in Fig. 1. The framework leverages a labeled dataset $D_l = \{(x_i, y_i)\}_{i=1}^{n_l}$ and a significantly larger unlabeled dataset $D_u = \{x_i\}_{i=n_l+1}^{n_l+n_u}$ to train the proposed model. Central to the design are four standard segmentation networks ($U1$, $U2$, $U3$, and $U4$), which are systematically optimized using a combination of MT training, prototype consistency alignment, CST, and the innovative edge replacement augmentation technique. The ultimate goal is to develop a robust segmentation model ($U4$) capable of precise meniscus delineation from MR images. The training paradigm integrates both labeled and unlabeled data, achieving high performance with an annotation ratio as low as 10%. Notably, $U2$ is refined through an exponential moving average (EMA) of $U1$'s weights. At inference, $U4$ directly outputs meniscus segmentations without requiring augmentation.

Three foundational innovations underpin the ERANet framework: (a) Edge Replacement Augmentation: ERA introduces structural variability by simulating meniscal shape variations. This is achieved by replacing the peripheral regions of the meniscus with background information (Fig. 1), thereby enhancing model robustness to morphological variations. (b) Prototype Consistency Alignment: This method strengthens intra-class feature similarity through prototype-based alignment. By computing correlations between prototypes and feature maps, it refines feature representations, while a prototypical consistency loss applied to unlabeled data fosters intra-class compactness. Cosine similarity serves as a pseudo-labeling mechanism to guide segmentation predictions. (c)

Conditional Self-Training: This component advances segmentation accuracy by incorporating stable pseudo labels derived from $U1$'s predictions across multiple checkpoints. Unlabeled images demonstrating consistent predictions are included in the labeled training set for $U3$, thereby iteratively enhancing model performance. Two rounds of self-training are employed to maximize gains in segmentation precision.

As depicted in Fig. 1, $U1$ and $U2$ form the mean-teacher architecture, trained on both labeled and unlabeled images. ERA is applied as a specific augmentation technique for labeled images, while PCA is used to align feature representations from unlabeled images. During the training process, CST aids in selecting reliable unlabeled images. $U3$ is supervised, and trained on both labeled and reliable unlabeled images (with pseudo labels generated by $U1$), benefiting from increased segmentation confidence for previously unreliable unlabeled images through ST. Finally, $U4$ incorporates the remaining unlabeled images, fully exploiting the dataset's potential and further refining model performance. Using the proposed method, we concurrently perform tibial cartilage segmentation, as it is essential for downstream quantification tasks, including the calculation of meniscus thickness. Nevertheless, the performance evaluation is exclusively focused on meniscus segmentation metrics. Comprehensive methodological details and experimental results are provided in the following sections.

3.2 Edge Replacement Augmentation

We propose a novel data augmentation strategy, Edge Replacement Augmentation, which is both conceptually simple and highly effective. The central objective of ERA is to simulate the variations in meniscal morphology often observed in knee OA. This is achieved by replacing the peripheral regions of the meniscus with background information extracted from the same image. Unlike conventional augmentation methods such as Copy-Paste [54], which transfer image patches between distinct images, ERA implements intra-image augmentation. It achieves this by sampling pixel values from the background regions adjacent to the meniscus and generating random values within the estimated pixel intensity range of these regions to replace the marginal areas of the meniscus.

This strategy introduces structural variability into the training data, thereby enhancing the robustness of segmentation models to anatomical variations. In our ERANet framework, ERA is incorporated into the MT configuration for $U1$ training, creating a "weak-to-strong" augmentation pipeline that facilitates consistency learning. Additionally, ERA is applied as a strong perturbation during $U3$'s ST process, ensuring further refinement of model predictions. Despite its simplicity, this approach yields substantial performance improvements when applied to models.

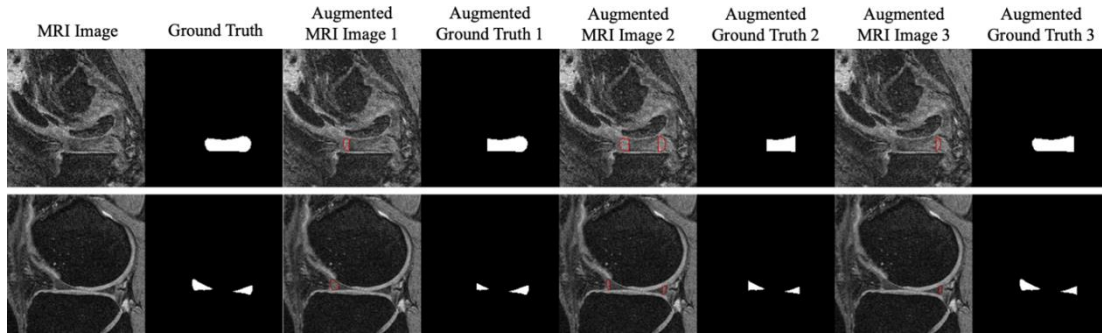


Figure 2. Representative examples of knee MRI images from the 3D DESS sequence alongside their edge-replaced augmented versions.

The example edge-replaced augmented images are presented in Fig. 2. For implementing ERA on labeled MR images, two scenarios are considered based on the anatomical configuration of the meniscus in the image X : (1) a single meniscal piece, referred to as *type A*, shown in the first row of Fig. 2, and (2) two distinct meniscal pieces, referred to as *type B*, depicted in the second row of Fig. 2. The augmentation process follows these steps:

- Mask Generation**

For labeled examples, given a knee MRI image X and its corresponding segmentation label L , a binary mask $M \in \{0, 1\}$ is created. In this mask, $M = 1$ identifies pixels corresponding to the meniscus, while $M = 0$ represents the background. Subsequently, duplicate the image and mask to obtain X_{ERA} and M_{ERA} , which will serve as the augmented counterparts.

- Identification of Extreme Points**

The extreme points along the outer curve of the meniscus in M are identified as follows:

- Far-left point (P_{FL}), upper-left point (P_{UL}), and bottom-left point (P_{BL}).

- Far-right point (P_{FR}), upper-right point (P_{UR}), and bottom-right point (P_{BR}).

For *type A* images (single meniscal piece), these points pertain to the single meniscus. For *type B* images (two separate meniscal pieces), P_{FL} , P_{UL} , P_{BL} correspond to the left meniscal piece, and P_{FR} , P_{UR} , P_{BR} to the right.

3. Meniscus Distance and Replacement Point Selection

- The distance d between P_{FL} and P_{FR} is measured for *type A* images. For *type B* images, the distances d_L and d_R are calculated for the respective pieces.
- Replacement points P_{RL} and P_{RR} are randomly selected as follows:
 - type A* images:

$$P_{RL} \in (x_{FL}, x_{FL} + 0.3d) \text{ and } P_{RR} \in (x_{FR} - 0.3d, x_{FR})$$
 - type B* images:

$$P_{RL} \in (x_{FL}, x_{FL} + 0.3d_L) \text{ and } P_{RR} \in (x_{FR} - 0.3d_R, x_{FR})$$

where x represents the x -coordinate of the point.

4. Edge-Replaced Image Generation

- **Bounding Box Construction:**
 Two bounding boxes are defined to encompass the marginal meniscus regions.

$$BB_{ox_L} = ((x_{FL} - 5, y_{BL}), (\max(x_{UL}, x_{BL}), y_{UL}))$$

$$BB_{ox_R} = ((\min(x_{UR}, x_{BR}), y_{BR}), (x_{FR} + 5, y_{UR})).$$
- **Region Cropping:**
 Using these bounding boxes, the image X and mask M are cropped to produce X_{CL} , X_{CR} , M_{CL} , and M_{CR} , corresponding to the left and right regions of the marginal meniscus, including surrounding tissues.
- **Background Creation:**
 Perform element-wise multiplication to remove the meniscus:

$$X_{CBL} = X_{CL} \times (1 - M_{CL}) \text{ and } X_{CBR} = X_{CR} \times (1 - M_{CR}),$$
 yielding background-only regions. The pixel value ranges R_L and R_R are then calculated for X_{CBL} and X_{CBR} , respectively.
- **Pixel Replacement:**
 For pixels with x -coordinate $x < x_{RL}$, where x_{RL} is the x -coordinate of P_{RL} , fill values using random samples from R_L in X_{ERA} .
 For pixels with x -coordinate $x > x_{RR}$, where x_{RR} is the x -coordinate of P_{RR} , fill values using random samples from R_R in X_{ERA} .

5. Edge-Replaced Mask Generation

- For pixels with x -coordinate $x < x_{RL}$, where x_{RL} is the x -coordinate of P_{RL} , set zero in M_{ERA} .
- For pixels with x -coordinate $x > x_{RR}$, where x_{RR} is the x -coordinate of P_{RR} , set zero in M_{ERA} .

X_{ERA} and M_{ERA} are the resulting augmented image and annotation respectively.

3.3 Prototype Consistency Alignment

3.3.1 Mean Teacher

The MT method is a semi-supervised learning approach that enhances segmentation by enforcing prediction consistency across augmented inputs while leveraging large unlabeled datasets [32]. It consists of a student network ($U1$) and a teacher network ($U2$) with identical architectures. In our ERANet framework, the student network is defined as $f_{U1}(X_{ERA}^l, Y, X^u; \theta)$, and the teacher network as $f_{U2}(X^u; \theta')$, where $f(\cdot)$ represents the segmentation network, and θ, θ' are their parameters. The student is trained on both labelled (X^l) and unlabeled data X^u , with labeled examples augmented via ERA, while the teacher is updated through an EMA of the student's weights [32]. The teacher network provides pseudo labels for unlabeled data, guiding the student network toward robust predictions. The key mechanism, consistency regularization, minimizes discrepancies between student and teacher outputs on unlabeled data, improving segmentation accuracy and generalization.

3.3.2 Prototypical Consistency Loss

Prototype Consistency Alignment

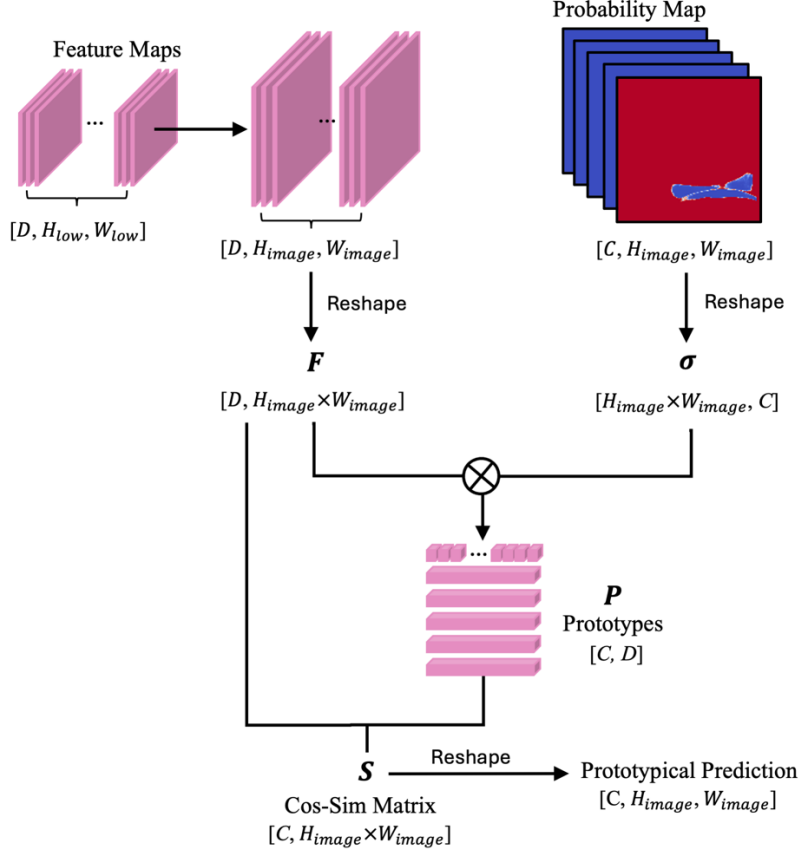


Figure 3. Detailed illustration of the prototypical consistency loss calculation.

Prototypes, as aggregated feature representations for each class, serve as condensed embeddings that encapsulate the defining characteristics of pixel-level features from input data. These prototypes act as class-specific feature centroids, guiding the segmentation network by leveraging the relationship between the prototypes and the input feature maps. Through the computation of correlations between prototypes and feature maps, the segmentation network reduces inter-class variability and enhances intra-class uniformity. In our framework, the similarity correlation maps are expressed as prototypical segmentation predictions, derived from the network's probability outputs and feature embeddings. This process is performed by UI on unlabeled images, with the calculation steps for a single image illustrated in Fig. 3. To generalize the methodology, the figure demonstrates the application of prototypical predictions for both cartilage and meniscus segmentation. Formally, σ denotes the output of the network. $F \in \mathbb{R}^{D \times H \times W}$ represents the feature map, where D corresponds to the depth of the final up-convolutional block in the U-Net architecture. The prototypes for all classes is computed as:

$$P = \frac{F \cdot \sigma}{H \times W} \odot \left(1_D \cdot \frac{1}{\sum_{i=1}^{H \times W} \sigma_i} \right) \quad (1)$$

This formulation ensures that the class prototype is calculated as a weighted average of feature embeddings, with weights determined by the network probabilities. By emphasizing regions with high confidence for class j , the prototype encapsulates the most discriminative characteristics of the class. This design not only enhances segmentation accuracy but also provides a robust mechanism for aligning feature spaces, which is critical for achieving high-quality results in semi-supervised settings. In each training iteration, UI computes $B \times C$ prototypes, where B denotes the batch size and C represents the number of segmentation classes. To rigorously assess the alignment between the prototypes and the feature maps, the cosine similarity is calculated as:

$$S = \frac{P^T \cdot F}{\|P\|^T \cdot \|F\|} \quad (2)$$

where $\frac{[]}{[]}$ denotes element-wise division, $\|P\| \in \mathbb{R}^{B \times C}$, and $\|F\| \in \mathbb{R}^{1, H \times W}$. The norms $\|P\|_j$ and $\|F\|_j$ are defined as:

$$\|P\|_j \equiv \sqrt{\sum_{d=1}^D P_{dj}^2}, \quad \|F\|_j \equiv \sqrt{\sum_{d=1}^D F_{dj}^2},$$

where j indexes the dimensions of class C . Since the prototype is aggregated from the features within example itself, it ensures that F aligns with more uniform feature representations, thereby promoting intra-class consistency in the segmentation predictions. This cosine similarity metric quantifies the angular alignment between the normalized feature embeddings and the corresponding class prototypes, reinforcing feature coherence and minimizing inter-class variance. To further promote intra-class cohesion and enhance segmentation accuracy, we propose a prototypical consistency loss to supervise the segmentation predictions.

$$L_{consis} = \sum_{j=1}^C \sum_i^{H \times W} (SS_{ij} - \sigma_{ij})^2 \quad (3)$$

where SS_{ij} is defined as $SOFTMAX(S_{ij})$.

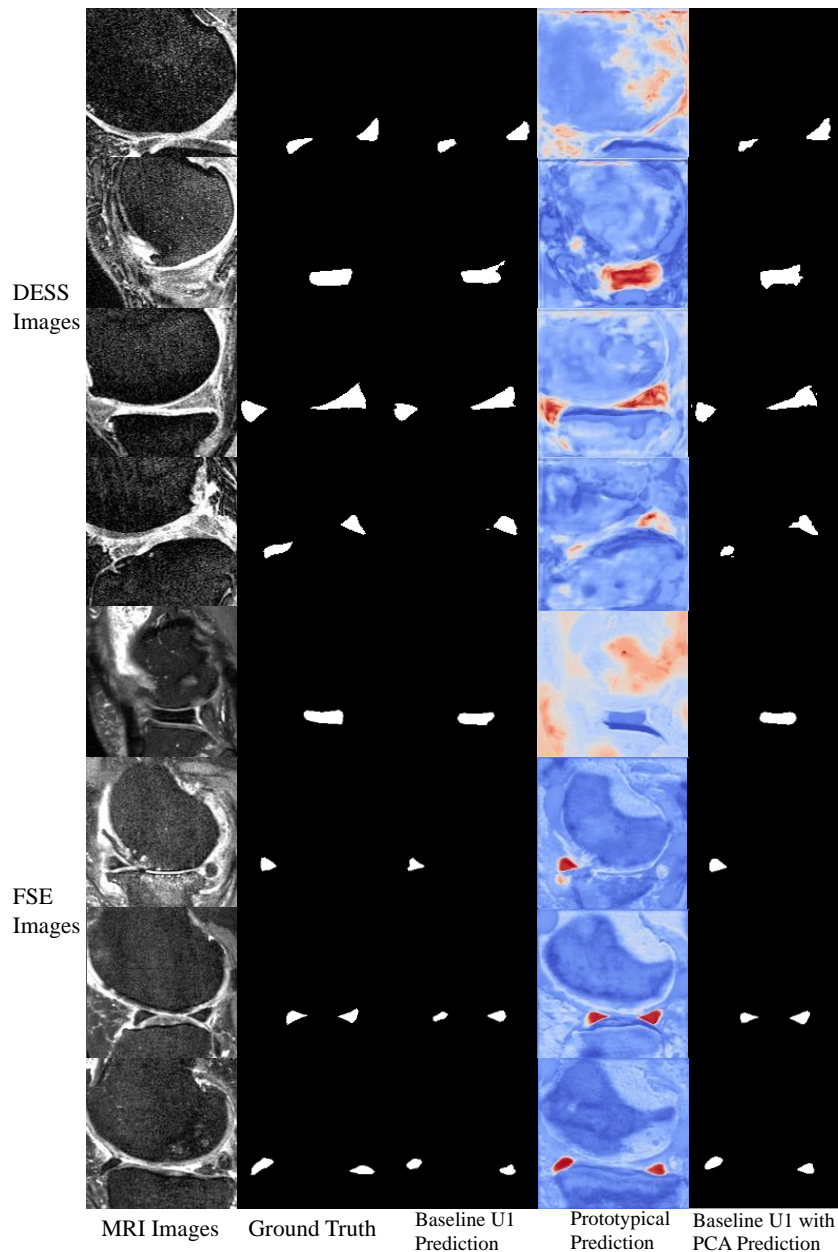


Figure 4. Representative examples of MRI images, including both DESS and FSE sequences, ground truth annotations of the meniscus, segmentation predictions from the baseline U1 model, and predictions from baseline U1 enhanced with PCA.

The incorporation of prototypical predictions supports the broader objective of minimizing reliance on labeled data by leveraging class-specific priors to refine segmentation outcomes, underscoring the potential of this methodology for advancing state-of-the-art segmentation techniques. Fig.4. illustrates the performance enhancement resulting from prototype consistency alignment.

3.4 Conditional Self-Training Strategy

The modified MT framework, incorporating ERA and prototype consistency alignment, demonstrates strong performance. However, traditional ST methods fail to differentiate between unlabeled samples of varying stability and difficulty, treating all samples uniformly during training [50, 55]. This limitation arises from the absence of ground truth for unlabeled data, where predictions by the $U1$ can often be inaccurate, resulting in noisy and unreliable pseudo labels for more challenging samples. Such pseudo labels, when included in training, can degrade overall model performance. To overcome this challenge, we propose a CST method that integrates a selective sampling strategy. This method emphasizes the inclusion of more reliable unlabeled samples by filtering out those with low-confidence predictions. Through two rounds of progressive ST, CST enables the efficient and safe utilization of the entire unlabeled dataset, adopting an incremental learning strategy that incorporates increasingly complex samples over time.

Building upon insights from [50], we assess the reliability of pseudo labels for each unlabeled image $x_i \in D_u$ by leveraging their progressive stability during training. Specifically, for K model checkpoints $\{M_j\}_{j=1}^K$ saved during the training process, we generate pseudo labels $\{O_{ij}^{U1}\}_{j=1}^K$ for x_i using predictions from the student network $U1$. We systematically saved five checkpoints at equidistant intervals, corresponding to 1/5, 2/5, 3/5, 4/5, and 5/5 of the total training iterations. As models generally converge and achieve peak performance in the later stages of training, we evaluate the Dice Similarity Coefficient (DSC) between earlier pseudo labels and the final pseudo-label to quantify prediction stability. The reliability score R_i for the pseudo-label of image x_i is computed as follows:

$$R_i = \frac{1}{K-1} \sum_{j=1}^{K-1} \left(\frac{2O_{ij}^{U1}O_{iK}^{U1}}{O_{ij}^{U1} + O_{iK}^{U1}} \right) \quad (4)$$

where R_i reflects the agreement between the intermediate pseudo labels $\{O_{ij}^{U1}\}_{j=1}^K$ and the final pseudo-label O_{iK}^{U1} . A higher R_i indicates greater stability and reliability.

Algorithm 1: CST Pseudocode

Input: D_l labeled training set, D_u unlabeled training dataset, strong augmentation ERA , threshold T , K checkpoints from $U1$ $\{M_j\}_{j=1}^K$
Output: Trained segmentation model $U4$
for $x_i \in D_u$ **do**
 for $M_j \in \{M_j\}_{j=1}^K$ **do**
 Predict pseudo-label $O_{ij}^{U1} = M_j(x_i)$
 Compute reliability score R_i for x_i using Equation (4).
 Select reliable samples $D_{sta} = \{x_k \mid R_k \geq T, x_k \in D_u\}$
 Set $D_{unsta} = D_u \setminus D_{sta}$
 Train $U3$ on $D_l \cup \{(x_k, M_K(x_k)) \mid x_k \in D_{sta}\}$ with ERA
 Update pseudo labels for D_{unsta} using $U3$
 Train $U4$ on $D_l \cup \{(x_k, M_K(x_k)) \mid x_k \in D_{sta}\} \cup \{(x_k, U3(x_k)) \mid x_k \in D_{unsta}\}$
Return $U4$

With the computed reliability scores for all unlabeled samples, we apply a thresholding strategy to filter the dataset. Unlabeled images with reliability scores above a threshold of 0.8—indicating stable and confident predictions—are selected for the first ST stage. These reliable samples, combined with the labeled dataset, are used to train the segmentation model $U3$. Following this refinement, the improved segmentation model $U3$ is employed to generate updated pseudo labels for the remaining unreliable samples. The improvement in pseudo-labeling for unreliable unlabeled images using $U3$ is illustrated in Fig. 5. In the subsequent ST stage, the entire dataset—including both manually labeled and pseudo-labeled data—is utilized for further training of $U4$, allowing the model to effectively learn from the entire dataset while minimizing the influence of noisy labels. The CST framework offers significant advantages by systematically incorporating stability metrics into the ST process. The pseudocode for the proposed CST method is detailed in Algorithm 1.

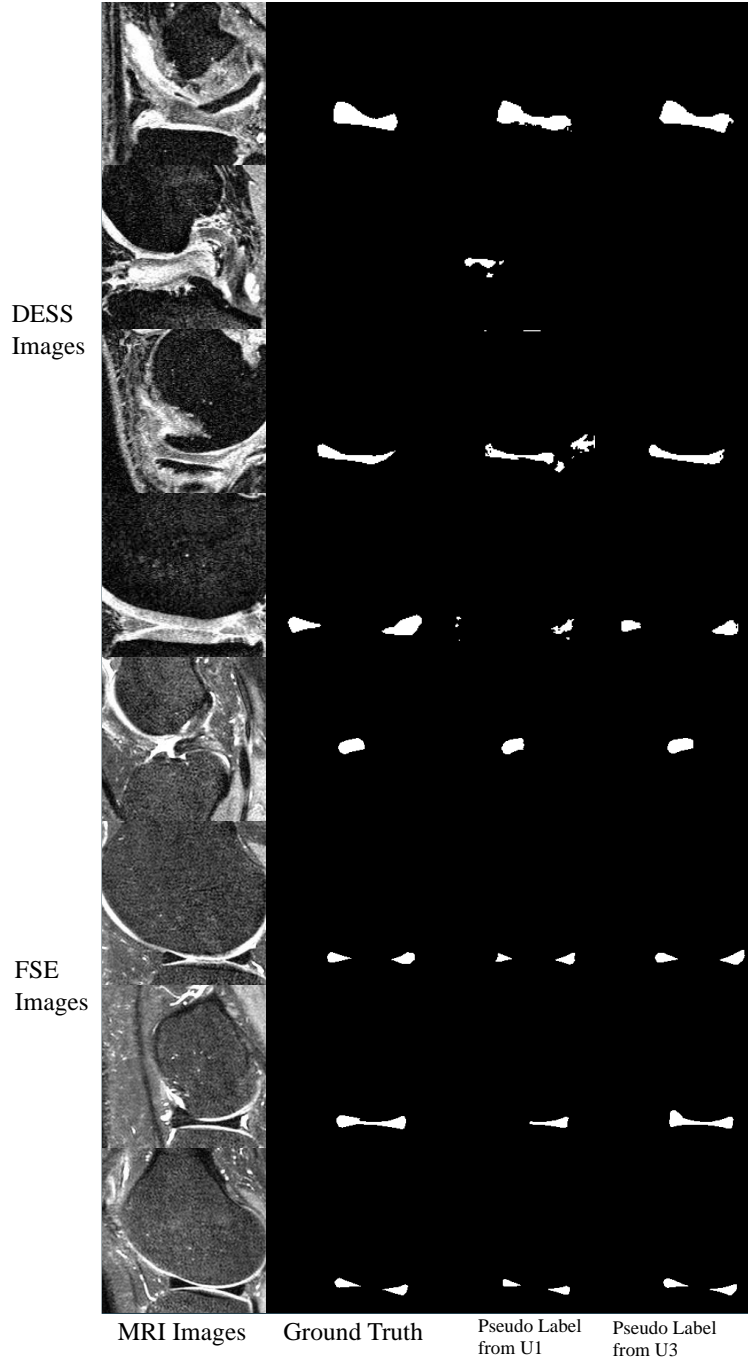


Figure 5. Representative examples of DESS and FSE MRI images, ground truth annotations for the meniscus, pseudo labels generated by the U1 model, and pseudo labels generated by the U3 model for unreliable unlabeled images.

3.5 Loss Function for Each Segmentation Network

To train the proposed semi-supervised segmentation framework (illustrated in Fig. 1), we define the loss functions for each network as follows. The loss function for the student network U1 is given by:

$$L_{U1} = L_{sup}^{U1} + \lambda L_{consis} + L_{unsup} \quad (5)$$

where L_{sup} represents the supervised loss, which combines the DSC and cross-entropy loss for the labeled images. The prototypical consistency loss is weighted by a time-dependent factor λ , defined as:

$$\lambda(t) = 0.1 * e^{\left(-10\left(1-\frac{E}{E_{max}}\right)\right)^2} \quad (6)$$

where E denotes the current epoch, and E_{max} is the maximum epoch. The unsupervised loss L_{unsup} measures the cross-entropy between the segmentation predictions from networks U2 and U1 on unlabeled image. For the segmentation network U3, the loss function L_{U3} consists solely of the supervised loss, computed on the renewed labeled dataset. This dataset includes both the true labeled training data and the reliable pseudo-labeled data generated from previous models. For the segmentation network U4, the loss function L_{U4} also consists solely of the supervised loss, calculated on the entire labeled dataset combined with the pseudo-labeled dataset. For reliable unlabeled images, pseudo labels are generated by U1, while for unreliable unlabeled images, updated pseudo labels are provided by U3. Both L_{U3} and L_{U4} utilize a combination of DSC and cross-entropy losses.

4. Experiments and Results

4.1 Datasets

We evaluated the performance of our semi-supervised segmentation models using two distinct datasets: the publicly available OAI-iMorphics dataset and an in-house dataset. The OAI-iMorphics dataset consists of 176 MR examinations, acquired using a 3.0T Siemens MAGNETOM Trio scanner (Siemens Healthcare, Erlangen, Germany) with a sagittal 3D DESS water excitation imaging sequence. This dataset is publicly accessible via the Osteoarthritis Initiative (OAI) repository at <http://www.oai.ucsf.edu>. The relevant imaging parameters for this dataset include a repetition time (TR) of 16.3 ms, an echo time (TE) of 4.7 ms, a flip angle of 25°, a voxel size of $0.365 \times 0.465 \times 0.7$ mm, a matrix size of 307×384 , a field of view (FOV) of 140 mm, and 160 image slices. Further details can be found on the OAI website. Manual annotations for the knee joint regions were performed in the sagittal plane by two musculoskeletal radiologists, covering six distinct sub-regions: femoral cartilage, lateral tibial cartilage, medial tibial cartilage, patellar cartilage, lateral meniscus, and medial meniscus. For our experiments, we excluded the femoral and patellar cartilage regions, as they were not directly relevant to meniscus quantification. The dataset was randomly split into 140 subjects for training and 36 subjects for testing.

The in-house dataset consists of 33 knee MRI scans of patients with OA. The dataset was collected in 2021 at the Prince of Wales Hospital in Sha Tin, New Territories, Hong Kong SAR, China. These scans were acquired using a Philips Achieva TX 3.0T scanner (Philips Healthcare, Best, Netherlands) with a 3D FSE/TSE (VISTA™) sequence. The study was approved by the institutional review board. Among the 33 patients, 12 were classified as Kellgren-Lawrence (KL) grade 1, 9 as KL grade 2, 5 as KL grade 3, and 7 as KL grade 4. Severe OA cases (KL grade 3 and 4) make meniscus segmentation more challenging due to reduced contrast between meniscus and surrounding tissues. The imaging parameters for this dataset include a TR of 1200 ms, a TE of 32 ms, an acquisition voxel size of $0.55 \times 0.545 \times 0.55$ mm and interpolated to a reconstruction voxel size of $0.29 \times 0.29 \times 0.55$ mm, a matrix size of 236×276 , and 292 image slices. The same six sub-regions (femoral cartilage, lateral tibial cartilage, medial tibial cartilage, patellar cartilage, lateral meniscus, and medial meniscus) were manually annotated by an experienced researcher and a radiologist with over 10 years of expertise. The dataset was randomly divided into 27 subjects for training and 6 subjects for testing.

In the context of our semi-supervised experiments, we treated some of the annotated training data as unannotated. Prior to model training, we pre-processed the images using histogram equalization and normalization techniques to improve image contrast and standardize the intensity distributions across the dataset. Two widely adopted metrics in medical image segmentation, the DSC and average symmetric surface distance (ASSD), were utilized to assess the quality of the experimental results.

4.2 Implementation details

The proposed semi-supervised segmentation framework was implemented in Python 3.9.7 with PyTorch 2.4.0. All experiments were conducted on two NVIDIA RTX A6000 GPUs, each equipped with 48 GB of memory, operating in parallel. The networks were initialized using Kaiming’s normal initialization method. Consistent hyperparameters were maintained across the training of $U1$, $U3$, and $U4$. The Adam optimizer was used for training all networks, with an initial learning rate of 0.01. A polynomial decay schedule, defined as $lr = baselr(1 - \frac{epoch}{total_epoch})^{0.9}$, was employed to reduce the learning rate progressively. Each network was trained for 200 epochs with a batch size of 8, and these configurations were applied uniformly to both the OAI-iMorphics and the in-house datasets. To enhance the model’s robustness against edge irregularities, strong data augmentations through ERA were applied to the unlabeled images during the training of $U1$ and $U3$. For computational efficiency, all images were cropped to a resolution of 256×256 pixels. Model training and evaluations were performed on a system powered by CUDA 11.5, enabling efficient accelerated computations.

4.3 Performances of the proposed semi-supervised framework

Our proposed framework consists of four networks—U1, U2, U3, and U4—designed for meniscus segmentation from MR images, with the final segmentation results provided by the desired network, U4. Table 1 presents the quantitative evaluations of the segmentation performance of the proposed framework across the OAI-iMorphics and the in-house datasets. For the OAI-iMorphics dataset, the UNet model achieved optimal performance with a mean DSC of 88.95% when trained on the full set of labeled data. However, when the labeled data was reduced to 10% (n=14), the performance of baseline U1 model significantly declined, with the mean DSC dropping to 83.48%, highlighting the adverse effects of limited labeled data. The term “baseline U1” in the table refers to the UNet model trained exclusively on a small amount of labeled data, without the use of any unlabeled data or specialized training strategies. By leveraging 126 additional unlabeled scans through the proposed ERANet framework, the segmentation performance improved substantially, achieving a mean DSC of 86.66%. This represents a relative improvement of 3.8% over the baseline U1 model, demonstrating the effectiveness of incorporating unlabeled data.

For the in-house dataset, the UNet model trained on 27 labeled scans yielded a mean DSC of 73.12%. However, with only 3 labeled scans, the performance dropped dramatically, with the mean DSC falling to 50.38%. In this scenario, the integration of 24 unlabeled scans within the ERANet framework resulted in significant improvements, achieving a mean DSC of 64.33%. This corresponds to a relative improvement of 27.7% over the baseline U1 model trained with 3 labeled scans, highlighting the framework's ability to mitigate the challenges associated with limited labeled data, particularly in datasets characterized by greater complexity in imaging and anatomical structures. Across both datasets, the segmentation performance of the lateral meniscus consistently surpassed that of the medial meniscus, as evidenced by higher DSC values and lower ASSD values. These findings highlight the robustness and adaptability of the ERANet framework in handling diverse datasets and the scarcity of labeled data.

Table 1. Quantitative evaluation of segmentation performance of the UNet, Baseline U1, and the proposed framework. Baseline U1 refers to UNet model trained on a small amount of labelled data without the use of any unlabeled data.

| Dataset | Method | #scans used | | DSC (%) | | | ASSD (mm) | | |
|---------------|-------------|-------------|-----------|------------------|-----------------|-------|------------------|-----------------|-------|
| | | Labeled | Unlabeled | Lateral Meniscus | Medial Meniscus | Mean | Lateral Meniscus | Medial Meniscus | Mean |
| OAI-iMorphics | UNet | 140 | 0 | 90.63 | 87.26 | 88.95 | 0.14 | 0.20 | 0.17 |
| | Baseline U1 | 14 | 0 | 86.13 | 80.83 | 83.48 | 0.54 | 0.71 | 0.63 |
| | U4 (ERANet) | 14 | 126 | 88.86 | 84.46 | 86.66 | 0.22 | 0.43 | 0.33 |
| in-house | UNet | 27 | 0 | 82.47 | 63.76 | 73.12 | 0.51 | 2.23 | 1.37 |
| | Baseline U1 | 3 | 0 | 62.62 | 38.14 | 50.38 | 3.92 | 21.63 | 12.78 |
| | U4 (ERANet) | 3 | 24 | 78.14 | 50.51 | 64.33 | 1.31 | 7.39 | 4.35 |

4.4 Performance across Various Data Partitioning Strategies

This section evaluates the effectiveness of our proposed framework using a data partitioning approach, where the datasets are divided into labeled and unlabeled subsets with ratios of 1/n and (1-1/n), respectively. For the OAI-iMorphics dataset, the partitioning was applied with ratios of 1/20, 1/10, and 1/5. Due to the smaller size of the in-house dataset, the partitioning ratios used were 1/10, 1/5, and 1/2. Initially, we compared our approach with the fully supervised UNet, which was trained using the same labeled data ratios. Subsequently, we evaluated the performance of our proposed U1 and the final network, U4. U1 denotes the model enhanced with ERA and CST, building upon the baseline U1. The results of these evaluations for both datasets are summarized in Tables 2 and 3, respectively.

Table 2. Quantitative evaluation of the proposed method on the OAI-Imorphics dataset with different data partition protocols.

| Method | #scans used | | DSC (%) | | | ASSD | | |
|-------------|-------------|-----------|------------------|-----------------|--------------|------------------|-----------------|-------------|
| | Labeled | Unlabeled | Lateral Meniscus | Medial Meniscus | Mean | Lateral Meniscus | Medial Meniscus | Mean |
| Baseline U1 | 28 | 0 | 87.73 | 83.72 | 85.73 | 0.37 | 0.37 | 0.37 |
| U1 | | | 88.03 | 84.00 | 86.02 | 0.25 | 0.50 | 0.38 |
| U4 (ERANet) | 28 | 112 | 88.98 | 85.15 | 87.07 | 0.22 | 0.41 | 0.32 |
| Baseline U1 | 14 | 0 | 86.13 | 80.83 | 83.48 | 0.54 | 0.71 | 0.63 |
| U1 | | | 88.01 | 82.94 | 85.48 | 0.22 | 0.54 | 0.38 |
| U4 (ERANet) | 14 | 126 | 88.86 | 84.46 | 86.66 | 0.22 | 0.43 | 0.33 |
| Baseline U1 | 7 | 0 | 83.29 | 76.82 | 80.01 | 0.59 | 1.36 | 0.98 |
| U1 | | | 86.59 | 81.49 | 84.04 | 0.31 | 0.79 | 0.55 |
| U4 (ERANet) | 7 | 133 | 87.52 | 83.28 | 85.40 | 0.22 | 0.35 | 0.29 |

As shown in Table 2 for the OAI-iMorphics dataset, when trained with 1/5 of the labeled scans, the U1 network, which incorporated 112 unlabeled scans, demonstrated a slight improvement, achieving a mean DSC of 86.02%, up from 85.73% achieved by the UNet. The proposed ERANet further enhanced segmentation performance, attaining the highest mean DSC of 87.07%. Reducing the labeled data to 1/10 of the scans led to a decline in the UNet’s performance, with a mean DSC of 83.48%. By leveraging 126 unlabeled scans, the U1 network improved the mean DSC to 85.48%. However, ERANet surpassed both models, achieving a mean DSC of 86.66%, underscoring its ability to effectively utilize unlabeled data to compensate for the reduction in labeled data. In the most challenging scenario, where only 7 labeled scans were available, the UNet achieved a mean DSC of 80.01%. By integrating 133 unlabeled scans, the U1 network improved to a mean DSC of 84.04%. Remarkably, ERANet excelled under these conditions, achieving a mean DSC of 85.40%, demonstrating its strong performance and potential in scenarios with minimal labeled data.

As the availability of labeled data decreased, the performance of the UNet declined markedly, reflecting the inherent challenges of training with limited annotations. In contrast, ERANet consistently mitigated this decline by leveraging unlabeled data, delivering substantial performance gains even in low-label settings. For instance, with only 7 labeled scans, ERANet achieved a mean DSC of 85.40%, significantly outperforming the UNet. These results emphasize ERANet’s effectiveness in addressing the limitations of sparse annotations for meniscus segmentation. Its capacity to utilize unlabeled data efficiently positions it as a promising solution for improving segmentation accuracy in resource-constrained medical imaging environments.

Table 3 illustrates the performance of the models on the in-house dataset under varying proportions of labeled and unlabeled data. With 14 labeled scans, UNet achieved a mean DSC of 62.68%. The addition of 13 unlabeled scans enhanced the performance, with U1 achieving a mean DSC of 69.00%. ERANet further improved the outcome, reaching a mean DSC of 72.17%. When the labeled data was reduced to 5 scans, UNet’s mean DSC dropped to 59.77%. However, incorporating 22 unlabeled scans into U1 increased the mean DSC to 65.42%, with ERANet outperforming both models at 67.09%. In the most challenging scenario, with only 3 labeled scans, UNet achieved a mean DSC of 50.38%. The inclusion of 24 unlabeled scans elevated U1’s performance to a mean DSC of 60.73%. ERANet again demonstrated superior results, achieving a mean DSC of 64.33%. These findings underscore ERANet’s effectiveness in leveraging unlabeled data to improve segmentation accuracy, particularly in settings with limited labeled examples.

Table 3. Quantitative evaluation of the proposed method on the in-house dataset with different data partition protocols.

| Method | #scans used | | DSC (%) | | | ASSD | | |
|-------------|-------------|-----------|------------------|-----------------|--------------|------------------|-----------------|-------------|
| | Labeled | Unlabeled | Lateral Meniscus | Medial Meniscus | Mean | Lateral Meniscus | Medial Meniscus | Mean |
| Baseline U1 | 14 | 0 | 75.81 | 49.54 | 62.68 | 1.62 | 6.26 | 3.94 |
| U1 | | | 80.75 | 57.26 | 69.01 | 0.66 | 4.15 | 2.41 |
| U4 (ERANet) | 14 | 13 | 81.08 | 63.25 | 72.17 | 0.79 | 2.09 | 1.44 |
| Baseline U1 | 5 | 0 | 72.00 | 47.53 | 59.77 | 1.51 | 6.17 | 3.84 |
| U1 | | | 78.64 | 52.19 | 65.42 | 0.73 | 5.69 | 3.21 |
| U4 (ERANet) | 5 | 22 | 78.17 | 56.01 | 67.09 | 1.06 | 5.66 | 3.36 |
| Baseline U1 | 3 | 0 | 62.62 | 38.14 | 50.38 | 3.92 | 21.63 | 12.78 |
| U1 | | | 73.49 | 47.96 | 60.73 | 2.59 | 10.6 | 6.60 |
| U4 (ERANet) | 3 | 24 | 78.14 | 50.51 | 64.33 | 1.31 | 7.39 | 4.35 |

4.5 Segmentation Performances Comparison with other stage-of-the-arts semi-supervised methods

In this section, we compare our proposed semi-supervised segmentation framework with several state-of-the-art methods in the field. These methods include MT [32], UA-MT [56], AdvChain [57], CTCT [28], CLD [58], and SCP-Net [49]. Among these, UA-MT is one of the most widely used MT-based frameworks for semi-supervised segmentation, leveraging uncertainty estimation to refine pseudo labels. AdvChain enhances model robustness by incorporating adversarial data augmentation techniques including random noise, random bias field affine transformations, and diffeomorphic deformations. CTCT utilizes consistency regularization via co-training, improving learning stability. CLD was specifically designed to address the class imbalance issue in knee MRI segmentation. SCP-Net, a prototype-based approach, integrates both self-aware and cross-sample prototypes, improving performance by considering intra- and inter-class variations. Each of these methods offers a unique contribution to the field of semi-supervised segmentation, and we benchmark them against our proposed framework to evaluate its effectiveness. Tables 4 and 5 present the corresponding comparison results for two distinct datasets.

Table 4. Comparison of the proposed framework's performance with other semi-supervised segmentation methods on the OAI-iMorphics dataset.

| Method | DSC (%) | | | ASSD | | |
|---------------|------------------|-----------------|--------------|------------------|-----------------|------|
| | Lateral Meniscus | Medial Meniscus | Mean | Lateral Meniscus | Medial Meniscus | Mean |
| MT [32] | 86.04 | 81.90 | 83.97 | 0.41 | 0.98 | 0.70 |
| UA-MT [56] | 87.09 | 83.03 | 85.06 | 0.26 | 0.40 | 0.33 |
| AdvChain [57] | 88.31 | 83.61 | 85.96 | 0.19 | 0.37 | 0.28 |
| CTCT [28] | 86.44 | 81.74 | 84.09 | 0.44 | 0.65 | 0.55 |
| CLD [58] | 87.90 | 83.71 | 85.81 | 0.33 | 0.37 | 0.35 |
| SCP-Net [49] | 87.26 | 81.98 | 84.62 | 0.48 | 0.78 | 0.63 |
| ERANet (Ours) | 88.86 | 84.46 | 86.66 | 0.22 | 0.43 | 0.33 |

As Table 4 shows for the OAI-iMorphics dataset, our proposed method, ERANet, achieves the best performance with an average DSC of 86.66%. Compared with other state-of-the-art semi-supervised segmentation methods, ERANet demonstrates superior accuracy in segmenting both the lateral and medial meniscus, consistently outperforming existing methods in DSC. Among the other semi-supervised approaches, AdvChain, which incorporates adversarial data augmentation, outperforms regularization-based methods and demonstrates a slight improvement in ASSD. This reflects the importance of data augmentation when the model already has a certain level of segmentation capability. By jointly optimizing the data augmentation process and the segmentation network during training, challenging examples are generated, which enhances the model's generalizability for downstream tasks. However, implementing dynamic data augmentation requires significant computational resources. In contrast, our proposed framework leverages three crucial techniques (reviewed in Section 3) to

effectively utilize limited labeled data and a substantial amount of unlabeled data: simulating meniscus variation through tailored data augmentation, aligning prototypical features, and selective self-training. These strategies likely contribute to the superior performance of ERANet, even when only limited labeled scans are available. The representative segmentation results from different methods are presented in Figure 6.

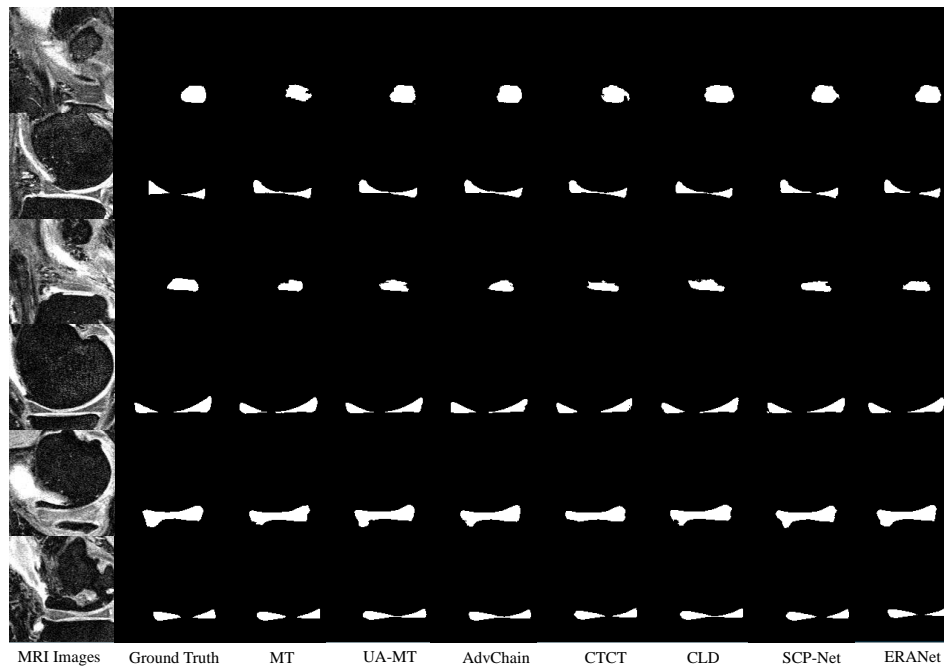


Figure 6. Segmentation results predicted by various state-of-the-art networks on the OAI-iMorphics dataset. From left to right: MRI Image, Ground Truth, and segmentation results from “MT,” “UA-MT,” “AdvChain,” “CTCT,” “CLD,” “SCP-Net,” and the proposed method.

The comparison results with other semi-supervised state-of-the-art methods for the in-house dataset are shown in Table 5. Similar to the OAI-iMorphics dataset, our proposed method, ERANet, achieves the best performance with an average DSC of 67.09%. The segmentation performance for the FSE sequence is lower than that for the DESS sequence, which can be attributed to the smaller amount of labeled data available for the FSE dataset, with only 5 labeled scans used for training. Additionally, the FSE dataset contains 36.4% of severe OA patients with a KL grade greater than 2. This introduces greater variability in the data, leading to higher discrepancies in the results from other methods. Compared with other semi-supervised methods, AdvChain also demonstrates its superiority due to its adversarial data augmentation technique. However, ERANet outperforms all models, likely due to the combination of data augmentation and feature alignment techniques that take full advantage of both labeled and unlabeled data. The representative segmentation results from different methods are presented in Figure 7.

Table 5. Comparison of the proposed framework’s performance with other semi-supervised segmentation methods on the in-house dataset.

| Method | DSC (%) | | | ASSD | | |
|----------------------|------------------|-----------------|--------------|------------------|-----------------|------|
| | Lateral Meniscus | Medial Meniscus | Mean | Lateral Meniscus | Medial Meniscus | Mean |
| MT [32] | 75.32 | 46.65 | 60.99 | 1.17 | 6.40 | 3.79 |
| UA-MT [56] | 76.37 | 47.72 | 62.05 | 0.93 | 5.54 | 3.24 |
| AdvChain [57] | 77.89 | 54.26 | 66.08 | 1.83 | 5.28 | 3.56 |
| CTCT [28] | 74.69 | 48.74 | 61.72 | 1.88 | 14.32 | 8.1 |
| CLD [58] | 77.17 | 53.13 | 65.15 | 1.98 | 3.91 | 2.95 |
| SCP-Net [49] | 76.56 | 48.28 | 62.42 | 0.65 | 4.57 | 2.61 |
| ERANet (Ours) | 78.17 | 56.01 | 67.09 | 1.06 | 5.66 | 3.36 |

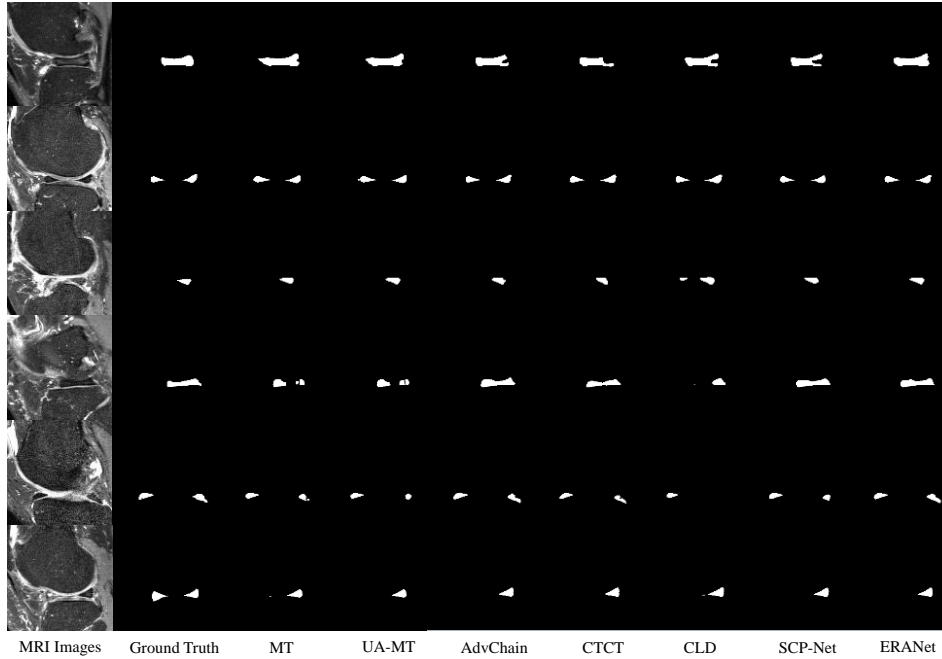


Figure 7. Segmentation results predicted by various state-of-the-art networks on the in-house dataset. From left to right: MRI Image, Ground Truth, and segmentation results from “MT,” “UA-MT,” “AdvChain,” “CTCT,” “CLD,” “SCP-Net,” and the proposed method.

4.6 Ablation Study

4.6.1. Edge Replacement Augmentation

As illustrated in Figures 8 and 9, edge replacement augmentation is integrated into the U1 and U3 networks to enhance segmentation of target tissues. Prototypical consistency loss and conditional self-training are applied as self-supervision techniques to refine the predictions of both models. Fig. 8 presents the performance of the U1 model under various augmentation strategies, including the absence of augmentation (“W/O Aug”) and the use of alternative advanced methods. “Strong Aug” encompasses random augmentations like Gaussian blur and color jittering, while advanced methods incorporate information from multiple images. For instance, “Mixup” creates new samples by linearly blending two examples and their labels, while variations such as CutMix replace rectangular regions of images, and Copy-Paste transfers specific object pixels. Similarly, Fig. 9 examines the U3 model’s performance under the same augmentation settings. The integration of ERA significantly improves the segmentation accuracy of both U1 (Fig. 8) and U3 (Fig. 9), yielding higher average DSC scores, especially for the medial meniscus. In Fig. 9, the baseline U3 model refers to the model trained using all reliable unlabeled data treated as pseudo-labeled data. This improvement can be attributed to the medial meniscus being more prone to injury compared to the lateral meniscus, with ERA introducing morphological variations that better mimic its structural diversity, thereby enhancing segmentation performance.

To further validate the effectiveness of ERA within ERANet, we assessed its impact on segmentation performance under varying ratios of annotated to unannotated data. The baseline U1 and U3 models were trained with and

without the inclusion of ERA. As shown in Fig. 10, the semi-supervised framework consistently demonstrated improved performance with the proposed ERA, regardless of the proportion of annotated to unannotated data.

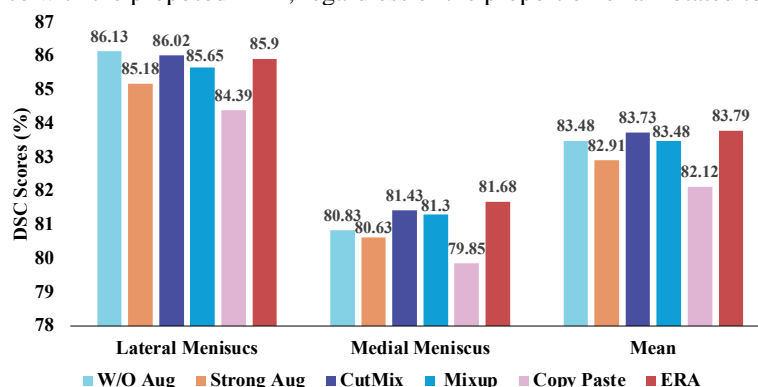


Figure 8. Quantitative evaluation of the baseline U1 model under various augmentation strategies. "Mean" refers to the average value calculated from the lateral meniscus and medial meniscus.

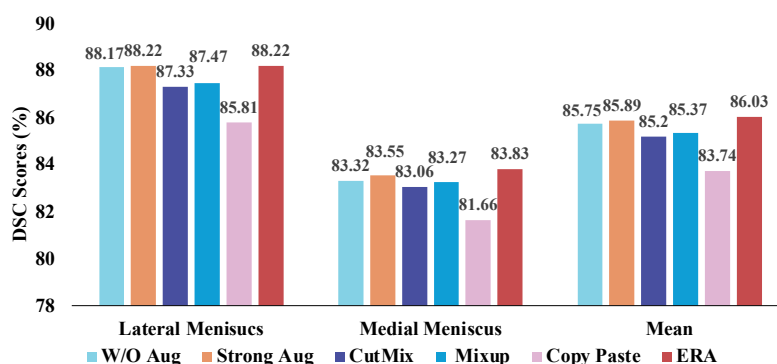


Figure 9. Quantitative evaluation of the baseline U3 model under various augmentation strategies. "Mean" refers to the average value calculated from the lateral meniscus and medial meniscus.

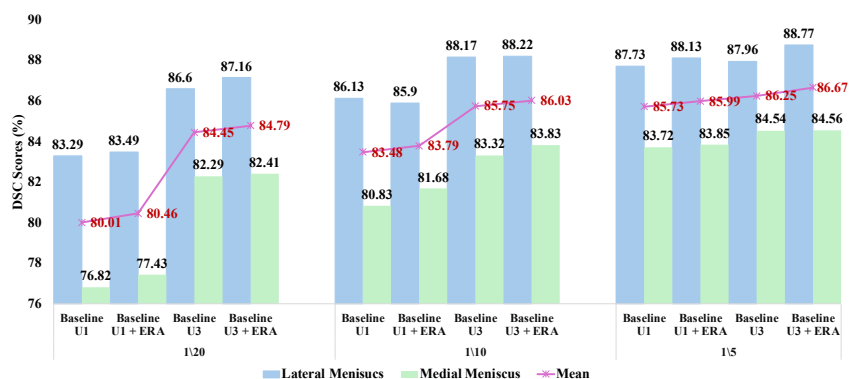


Figure 10. Impact of ERA on segmentation performance with varying ratios of annotated to unannotated data. "Mean" refers to the average value calculated from the lateral meniscus and medial meniscus.

4.6.2. Prototype Consistency Alignment

Building upon existing experiments, we evaluate the effectiveness of PCA by comparing the baseline U1 model trained with and without the PCA module. In the proposed framework, ERA has already been validated as a means to enhance meniscus segmentation performance through data perturbation. Therefore, we incorporate PCA on unlabeled images, building upon the foundation established by ERA. Note that the baseline U1 model, when equipped with ERA and PCA, corresponds to the U1 model presented in Table 2. Fig. 11 presents the comparison results under varying ratios of annotated to unannotated data. As shown in Fig. 11, the semi-supervised framework

consistently demonstrates improved performance with the proposed PCA, regardless of the ratio of annotated to unannotated data. Notably, the benefit of PCA becomes more pronounced as the number of labeled images decreases, highlighting its effectiveness in scenarios with limited annotated data.

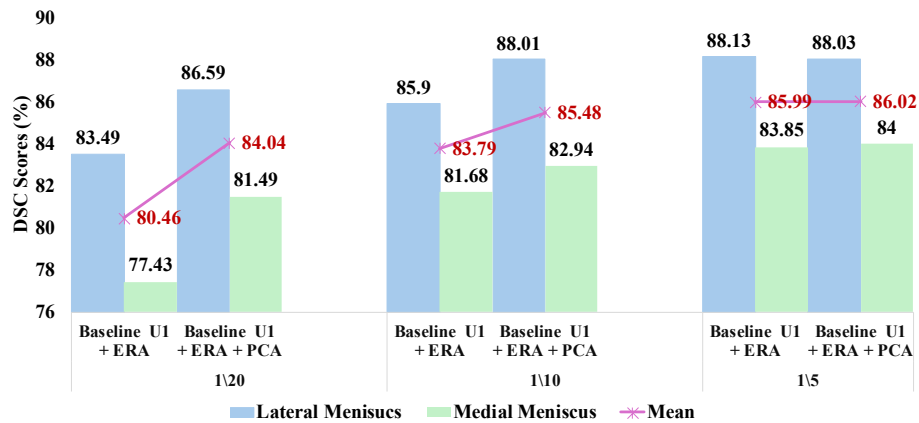


Figure 11. Comparison of segmentation performance for the U1 model with and without the prototype consistency alignment (PCA) module under varying ratios of annotated to unannotated data. "Mean" refers to the average value calculated from the lateral meniscus and medial meniscus.

4.6.3. Conditional Self-Training Strategy

To validate the effectiveness of CST within ERANet, we evaluated the impact of the two-stage iterative CST strategy on segmentation performance. The model is progressively optimized using a combination of manually labeled and pseudo-labeled images. As reported in Table 6, the semi-supervised framework consistently benefits from the proposed CST, irrespective of the ratio of annotated to unannotated data, highlighting CST's robustness and superior segmentation accuracy across varying annotation levels. Note that integrating CST into the baseline U3 model equipped with ERA results in the final proposed U4 model. Further analysis, detailed in Table 7, examines the improvements achieved at each stage of the CST process. During the first stage, where only a subset of the unlabeled images is used, the segmentation results surpass those of U1, underscoring the reliability of the selected pseudo labels. Ablation studies further reveal that the default DSC score threshold of 80% effectively balances performance, with ERANet demonstrating robustness to threshold variations.

Table 6. Quantitative comparison of segmentation performance between common ST and CST on the OAI-Imorphics dataset with different data partition protocols. The baseline U3 model equipped with ERA and CST is equivalent to the proposed ERANet.

| | #scans used | | DSC (%) | | | ASSD | | |
|---------------------|-------------|-------------|------------------|-----------------|--------------|------------------|-----------------|-------------|
| | Annotated | Unannotated | Lateral Meniscus | Medial Meniscus | Mean | Lateral Meniscus | Medial Meniscus | Mean |
| Baseline U3 + ERA | 28 | 112 | 88.77 | 84.56 | 86.67 | 0.25 | 0.38 | 0.32 |
| Baseline U3+ERA+CST | 28 | 112 | 88.98 | 85.15 | 87.07 | 0.22 | 0.41 | 0.32 |
| Baseline U3 + ERA | 14 | 126 | 88.22 | 83.83 | 86.03 | 0.27 | 0.37 | 0.32 |
| Baseline U3+ERA+CST | 14 | 126 | 88.86 | 84.46 | 86.66 | 0.22 | 0.43 | 0.33 |
| Baseline U3 + ERA | 7 | 133 | 87.16 | 82.41 | 84.79 | 0.30 | 0.51 | 0.41 |
| Baseline U3+ERA+CST | 7 | 133 | 87.52 | 83.28 | 85.40 | 0.22 | 0.35 | 0.29 |

Table 7. Training process of the proposed CST. CST initially trains the model on reliable unlabeled images (Self-training #1) and then on all pseudo-labeled images (Self-training #2). A quantitative comparison of segmentation performance during the CST training process on the OAI-Imorphics dataset with different data partition protocols.

| DSC threshold of reliable images | Stage | DSC (%) | | | ASSD | | |
|----------------------------------|------------------|------------------|-----------------|--------------|------------------|-----------------|-------------|
| | | Lateral Meniscus | Medial Meniscus | Mean | Lateral Meniscus | Medial Meniscus | Mean |
| 50% | Self-training #1 | 87.96 | 83.65 | 85.81 | 0.31 | 0.45 | 0.38 |
| | Self-training #2 | 88.38 | 84.10 | 86.24 | 0.25 | 0.51 | 0.38 |
| 60% | Self-training #1 | 88.10 | 83.88 | 85.99 | 0.26 | 0.38 | 0.32 |
| | Self-training #2 | 88.29 | 84.23 | 86.26 | 0.22 | 0.38 | 0.30 |
| 80% (default) | Self-training #1 | 88.34 | 83.88 | 86.11 | 0.25 | 0.42 | 0.34 |
| | Self-training #2 | 88.86 | 84.46 | 86.66 | 0.22 | 0.43 | 0.33 |
| 100% | Self-training #1 | 88.22 | 83.83 | 86.03 | 0.27 | 0.37 | 0.32 |
| | Self-training #2 | 88.29 | 84.62 | 86.46 | 0.27 | 0.43 | 0.35 |

5. Conclusion

In this study, we propose an effective semi-supervised framework that integrates edge replacement augmentation, prototype consistency alignment, and conditional self-training to enhance meniscus segmentation performance in knee MRI images. The framework utilizes both manually labeled and pseudo-labeled data, integrating edge replacement augmentation, prototypical consistency loss and conditional self-training employed as self-supervision strategies to refine model predictions. Extensive experiments were conducted on the OAI-Imorphics dataset and the in-house dataset, evaluating the proposed method's effectiveness across varying ratios of annotated to unannotated data. Our results show that the combination of ERA, prototype consistency alignment, and conditional self-training consistently improves segmentation accuracy, particularly for the medial meniscus.

Declaration of competing interest

The authors declare that there are no conflicts of interest regarding the publication of this paper.

CRedit authorship contribution statement

Siyue Li: Conceptualization; Data Curation; Formal Analysis; Investigation; Methodology; Software; Validation; Visualization; Writing-Original Draft; Writing - Review & Editing. **Yongcheng Yao**: Software; Validation; Investigation; Writing - Review & Editing. **Junru Zhong**: Validation; Data Curation; Investigation; Writing - Review & Editing. **Shutian Zhao**: Investigation; Data Curation; Writing - Review & Editing. **Fan Xiao**: Data Curation; Writing - Review & Editing. **Tim-Yun Michael Ong**: Data Curation; Resources; Writing - Review & Editing. **Ki-Wai Kevin Ho**: Data Curation; Resources; Writing - Review & Editing. **James F. Griffith**: Data Curation; Resources; Writing - Review & Editing. **Yudong Zhang**: Validation, Writing-Review & Editing. **Shuiua, Wang**: Validation, Writing Review & Editing. **Jin Hong**: Conceptualization, Investigation; Methodology; Funding Acquisition; Supervision; Writing-Review & Editing. **Weitian Chen**: Investigation; Methodology, Resources; Funding Acquisition; Project Administration; Supervision; Writing-Review & Editing.

Acknowledgments

This study was supported by in part by the National Natural Science Foundation of China (62466033), in part by the Jiangxi Provincial Natural Science Foundation (20242BAB20070) and a grant from the Innovation and Technology Commission of the Hong Kong SAR (Project No. MRP/001/18X). We would like to acknowledge Chi Yin Ben Choi and Cheuk Nam Cherry Cheng for their assistance in patient recruitment and MRI exams and Tsz Shing Adam Kwong for his assistance in data processing.

References

- [1] A. D. Woolf and B. Pfleger, "Burden of major musculoskeletal conditions," *Bulletin of the world health organization*, vol. 81, pp. 646-656, 2003.
- [2] C. R. Chu, A. A. Williams, C. H. Coyle, and M. E. Bowers, "Early diagnosis to enable early treatment of pre-osteoarthritis," *Arthritis research & therapy*, vol. 14, pp. 1-10, 2012.
- [3] T. Pollard, S. Gwilym, and A. Carr, "The assessment of early osteoarthritis," *The Journal of Bone & Joint Surgery British Volume*, vol. 90, pp. 411-421, 2008.
- [4] M. Favero, R. Ramonda, M. B. Goldring, S. R. Goldring, and L. Punzi, "Early knee osteoarthritis," *RMD open*, vol. 1, p. e000062, 2015.
- [5] H. Aoki, N. Ozeki, H. Katano, A. Hyodo, Y. Miura, J. Matsuda, *et al.*, "Relationship between medial meniscus extrusion and cartilage measurements in the knee by fully automatic three-dimensional MRI analysis," *Bmc Musculoskeletal Disorders*, vol. 21, Nov 12 2020.
- [6] N. Ozeki, H. Koga, and I. Sekiya, "Degenerative Meniscus in Knee Osteoarthritis: From Pathology to Treatment," *Life-Basel*, vol. 12, Apr 2022.
- [7] A. Wenger, M. Englund, W. Wirth, M. Hudelmaier, K. Kwok, F. Eckstein, *et al.*, "Relationship of 3D meniscal morphology and position with knee pain in subjects with knee osteoarthritis: a pilot study," *European Radiology*, vol. 22, pp. 211-220, Jan 2012.
- [8] M. Englund, "The role of biomechanics in the initiation and progression of OA of the knee," *Best practice & research Clinical rheumatology*, vol. 24, pp. 39-46, 2010.
- [9] F. W. Roemer, F. Eckstein, D. Hayashi, and A. Guermazi, "The role of imaging in osteoarthritis," *Best practice & research Clinical rheumatology*, vol. 28, pp. 31-60, 2014.
- [10] H. Liebl, "Analysis of the Osteoarthritis Initiative Incidence Cohort: Patellar Cartilage T2 and Focal Knee Pathology Derived from 3T MRI in Relation to Physical Activity," Technische Universität München, 2015.
- [11] Z. Zhou, G. Zhao, R. Kijowski, and F. Liu, "Deep convolutional neural network for segmentation of knee joint anatomy," *Magn Reson Med*, vol. 80, pp. 2759-2770, Dec 2018.
- [12] B. Norman, V. Padoia, and S. Majumdar, "Use of 2D U-Net Convolutional Neural Networks for Automated Cartilage and Meniscus Segmentation of Knee MR Imaging Data to Determine Relaxometry and Morphometry," *Radiology*, vol. 288, pp. 177-185, Jul 2018.
- [13] S. Gaj, M. R. Yang, K. Nakamura, and X. J. Li, "Automated cartilage and meniscus segmentation of knee MRI with conditional generative adversarial networks," *Magnetic Resonance in Medicine*, vol. 84, pp. 437-449, Jul 2020.
- [14] U. Jeon, H. Kim, H. Hong, and J. Wang, "Automatic Meniscus Segmentation Using Adversarial Learning-Based Segmentation Network with Object-Aware Map in Knee MR Images," *Diagnostics*, vol. 11, p. 1612, 2021.
- [15] Y. Z. Li, Y. Wang, K. B. Fang, H. Z. Zheng, Q. Q. Lai, Y. F. Xia, *et al.*, "Automated meniscus segmentation and tear detection of knee MRI with a 3D mask-RCNN," *European Journal of Medical Research*, vol. 27, Nov 14 2022.
- [16] G. Papandreou, L.-C. Chen, K. P. Murphy, and A. L. Yuille, "Weakly-and semi-supervised learning of a deep convolutional network for semantic image segmentation," in *Proceedings of the IEEE international conference on computer vision*, 2015, pp. 1742-1750.
- [17] Y. Grandvalet and Y. Bengio, "Semi-supervised learning by entropy minimization," *Advances in neural information processing systems*, vol. 17, 2004.
- [18] Y. Wang, H. Wang, Y. Shen, J. Fei, W. Li, G. Jin, *et al.*, "Semi-supervised semantic segmentation using unreliable pseudo-labels," in *Proceedings of the IEEE/CVF conference on computer vision and pattern recognition*, 2022, pp. 4248-4257.
- [19] Y. Li, J. Chen, X. Xie, K. Ma, and Y. Zheng, "Self-loop uncertainty: A novel pseudo-label for semi-supervised medical image segmentation," in *Medical Image Computing and Computer Assisted Intervention—MICCAI 2020: 23rd International Conference, Lima, Peru, October 4–8, 2020, Proceedings, Part I 23*, 2020, pp. 614-623.

- [20] K. Chaitanya, E. Erdil, N. Karani, and E. Konukoglu, "Local contrastive loss with pseudo-label based self-training for semi-supervised medical image segmentation," *Medical image analysis*, vol. 87, p. 102792, 2023.
- [21] R. Mendel, L. A. De Souza, D. Rauber, J. P. Papa, and C. Palm, "Semi-supervised segmentation based on error-correcting supervision," in *Computer Vision—ECCV 2020: 16th European Conference, Glasgow, UK, August 23–28, 2020, Proceedings, Part XXIX 16*, 2020, pp. 141-157.
- [22] C. Decourt and L. Duong, "Semi-supervised generative adversarial networks for the segmentation of the left ventricle in pediatric MRI," *Computers in Biology and Medicine*, vol. 123, p. 103884, 2020.
- [23] L. Zhang, A. Gooya, and A. F. Frangi, "Semi-supervised assessment of incomplete LV coverage in cardiac MRI using generative adversarial nets," in *Simulation and Synthesis in Medical Imaging: Second International Workshop, SASHIMI 2017, Held in Conjunction with MICCAI 2017, Québec City, QC, Canada, September 10, 2017, Proceedings 2*, 2017, pp. 61-68.
- [24] W.-C. Hung, Y.-H. Tsai, Y.-T. Liou, Y.-Y. Lin, and M.-H. Yang, "Adversarial learning for semi-supervised semantic segmentation," *arXiv preprint arXiv:1802.07934*, 2018.
- [25] Y. Ouali, C. Hudelot, and M. Tami, "Semi-supervised semantic segmentation with cross-consistency training," in *Proceedings of the IEEE/CVF conference on computer vision and pattern recognition*, 2020, pp. 12674-12684.
- [26] Y. Wu, Z. Ge, D. Zhang, M. Xu, L. Zhang, Y. Xia, *et al.*, "Mutual consistency learning for semi-supervised medical image segmentation," *Medical Image Analysis*, vol. 81, p. 102530, 2022.
- [27] X. Luo, J. Chen, T. Song, and G. Wang, "Semi-supervised medical image segmentation through dual-task consistency," in *Proceedings of the AAAI conference on artificial intelligence*, 2021, pp. 8801-8809.
- [28] X. D. Luo, M. H. Hu, T. Song, G. T. Wang, and S. T. Zhang, "Semi-Supervised Medical Image Segmentation via Cross Teaching between CNN and Transformer," *International Conference on Medical Imaging with Deep Learning, Vol 172*, vol. 172, pp. 820-833, 2022.
- [29] Y. Xia, D. Yang, Z. Yu, F. Liu, J. Cai, L. Yu, *et al.*, "Uncertainty-aware multi-view co-training for semi-supervised medical image segmentation and domain adaptation," *Med Image Anal*, vol. 65, p. 101766, Oct 2020.
- [30] X. Liu, F. Xing, N. Shusharina, R. Lim, C. J. Kuo, G. El Fakhri, *et al.*, "ACT: Semi-supervised Domain-adaptive Medical Image Segmentation with Asymmetric Co-Training," *Med Image Comput Assist Interv*, vol. 13435, pp. 66-76, Sep 2022.
- [31] H. Wu, B. Zhang, C. Chen, and J. Qin, "Federated Semi-Supervised Medical Image Segmentation via Prototype-Based Pseudo-Labeling and Contrastive Learning," *IEEE Trans Med Imaging*, vol. 43, pp. 649-661, Feb 2024.
- [32] A. Tarvainen and H. Valpola, "Mean teachers are better role models: Weight-averaged consistency targets improve semi-supervised deep learning results," *Advances in neural information processing systems*, vol. 30, 2017.
- [33] O. Ronneberger, P. Fischer, and T. Brox, "U-net: Convolutional networks for biomedical image segmentation," in *Medical image computing and computer-assisted intervention—MICCAI 2015: 18th international conference, Munich, Germany, October 5-9, 2015, proceedings, part III 18*, 2015, pp. 234-241.
- [34] S. Li, S. Zhao, Y. Zhang, J. Hong, and W. Chen, "Source-free unsupervised adaptive segmentation for knee joint MRI," *Biomedical Signal Processing and Control*, vol. 92, p. 106028, 2024.
- [35] A. Tack, A. Mukhopadhyay, and S. Zachow, "Knee menisci segmentation using convolutional neural networks: data from the osteoarthritis initiative," *Osteoarthritis and cartilage*, vol. 26, pp. 680-688, 2018.
- [36] U. Jeon, H. Kim, H. Hong, and J. H. Wang, "Automatic meniscus segmentation using cascaded deep convolutional neural networks with 2D conditional random fields in knee MR images," in *International Workshop on Advanced Imaging Technology (IWAIT) 2020*, 2020, pp. 412-415.
- [37] Z. Long, D. Zhang, H. Guo, and W. Wang, "Automated segmentation of knee menisci from magnetic resonance images by using ATTU-Net: a pilot study on small datasets," *OSA Continuum*, vol. 4, pp. 3096-3107, 2021.
- [38] S. Gaj, M. Yang, K. Nakamura, and X. Li, "Automated cartilage and meniscus segmentation of knee MRI with conditional generative adversarial networks," *Magnetic resonance in medicine*, vol. 84, pp. 437-449, 2020.
- [39] M. Byra, M. Wu, X. Zhang, H. Jang, Y. J. Ma, E. Y. Chang, *et al.*, "Knee menisci segmentation and relaxometry of 3D ultrashort echo time cones MR imaging using attention U-Net with transfer learning," *Magnetic resonance in medicine*, vol. 83, pp. 1109-1122, 2020.

- [40] E. Panfilov, A. Tiulpin, M. Juntunen, V. Casula, M. Nieminen, and S. Saarakkala, "Automatic knee cartilage and menisci segmentation from 3D-DESS MRI using deep semi-supervised learning," *Osteoarthritis and Cartilage*, vol. 27, pp. S390-S391, 2019.
- [41] Y. Xie, K. Jiang, Z. Zhang, S. Chen, X. Zhang, and C. Qiu, "Automatic segmentation of meniscus based on MAE self-supervision and point-line weak supervision paradigm," *arXiv preprint arXiv:2205.03525*, 2022.
- [42] J. Hou, X. Ding, and J. D. Deng, "Semi-supervised semantic segmentation of vessel images using leaking perturbations," in *Proceedings of the IEEE/CVF Winter Conference on Applications of Computer Vision*, 2022, pp. 2625-2634.
- [43] X. Chen, Y. Yuan, G. Zeng, and J. Wang, "Semi-supervised semantic segmentation with cross pseudo supervision," in *Proceedings of the IEEE/CVF Conference on Computer Vision and Pattern Recognition*, 2021, pp. 2613-2622.
- [44] Y. Xiao, C. Chen, X. Fu, L. Wang, J. Yu, and Y. Zou, "A novel multi-task semi-supervised medical image segmentation method based on multi-branch cross pseudo supervision," *Applied Intelligence*, vol. 53, pp. 30343-30358, 2023.
- [45] J. Liu, C. Desrosiers, and Y. Zhou, "Semi-supervised medical image segmentation using cross-model pseudo-supervision with shape awareness and local context constraints," in *International Conference on Medical Image Computing and Computer-Assisted Intervention*, 2022, pp. 140-150.
- [46] Y. Bai, D. Chen, Q. Li, W. Shen, and Y. Wang, "Bidirectional copy-paste for semi-supervised medical image segmentation," in *Proceedings of the IEEE/CVF conference on computer vision and pattern recognition*, 2023, pp. 11514-11524.
- [47] H. Xu, L. Liu, Q. Bian, and Z. Yang, "Semi-supervised semantic segmentation with prototype-based consistency regularization," *Advances in neural information processing systems*, vol. 35, pp. 26007-26020, 2022.
- [48] Z. Xu, Y. Wang, D. Lu, L. Yu, J. Yan, J. Luo, *et al.*, "All-Around Real Label Supervision: Cyclic Prototype Consistency Learning for Semi-Supervised Medical Image Segmentation," *IEEE J Biomed Health Inform*, vol. 26, pp. 3174-3184, Jul 2022.
- [49] Z. X. Zhang, R. Ran, C. N. Tian, H. Zhou, X. Li, F. Yang, *et al.*, "Self-aware and Cross-Sample Prototypical Learning for Semi-supervised Medical Image Segmentation," *Medical Image Computing and Computer Assisted Intervention, Miccai 2023, Pt Ii*, vol. 14221, pp. 192-201, 2023.
- [50] L. Yang, W. Zhuo, L. Qi, Y. Shi, and Y. Gao, "St++: Make self-training work better for semi-supervised semantic segmentation," in *Proceedings of the IEEE/CVF conference on computer vision and pattern recognition*, 2022, pp. 4268-4277.
- [51] J. Yuan, Y. Liu, C. Shen, Z. Wang, and H. Li, "A simple baseline for semi-supervised semantic segmentation with strong data augmentation," in *Proceedings of the IEEE/CVF International Conference on Computer Vision*, 2021, pp. 8229-8238.
- [52] Y. Zhu, Z. Zhang, C. Wu, Z. Zhang, T. He, H. Zhang, *et al.*, "Improving Semantic Segmentation via Efficient Self-Training," *IEEE Trans Pattern Anal Mach Intell*, vol. 46, pp. 1589-1602, Mar 2024.
- [53] B. Chen, L. Wang, X. Fan, W. Bo, X. Yang, and T. Tjahjadi, "Semi-FCMNet: Semi-supervised learning for forest cover mapping from satellite imagery via ensemble self-training and perturbation," *Remote Sensing*, vol. 15, p. 4012, 2023.
- [54] G. Ghiasi, Y. Cui, A. Srinivas, R. Qian, T.-Y. Lin, E. D. Cubuk, *et al.*, "Simple copy-paste is a strong data augmentation method for instance segmentation," in *Proceedings of the IEEE/CVF conference on computer vision and pattern recognition*, 2021, pp. 2918-2928.
- [55] X. Yang, Z. Song, I. King, and Z. Xu, "A survey on deep semi-supervised learning," *IEEE Transactions on Knowledge and Data Engineering*, vol. 35, pp. 8934-8954, 2022.
- [56] L. Q. Yu, S. J. Wang, X. M. Li, C. W. Fu, and P. A. Heng, "Uncertainty-Aware Self-ensembling Model for Semi-supervised 3D Left Atrium Segmentation," *Medical Image Computing and Computer Assisted Intervention - Miccai 2019, Pt Ii*, vol. 11765, pp. 605-613, 2019.
- [57] C. Chen, C. Qin, C. Ouyang, Z. J. Li, S. Wang, H. Q. Qiu, *et al.*, "Enhancing MR image segmentation with realistic adversarial data augmentation," *Medical Image Analysis*, vol. 82, Nov 2022.
- [58] Y. Q. Lin, H. F. Yao, Z. Z. Li, G. Y. Zheng, and X. M. Li, "Calibrating Label Distribution for Class-Imbalanced Barely-Supervised Knee Segmentation," *Medical Image Computing and Computer Assisted Intervention, Miccai 2022, Pt Viii*, vol. 13438, pp. 109-118, 2022.